A non-intrusive approach for enhancing power-system frequency stability

Tadej Skrjanc, *Student Member, IEEE*, Rafael Mihalic, *Member, IEEE* and Urban Rudez, *Member, IEEE*

Abstract
This paper presents a novel protection strategy for assuring power-system frequency stability. After many years of use, the existing (static) under-frequency load-shedding concept has proven to be reliable and fast. However, it does not adapt well to volatile operating conditions, which might often lead to a system collapse. This developed into a major obstacle, since operational conditions of modern power systems are persistently subjected to fast and unpredictable changes. Therefore, there is a need to introduce a new capability in under-frequency load-shedding that would be able to fine-tune the mismatch in active power in any conditions. From the practical aspect, a systematic implementation of improvements should not threaten system stability. In terms of cost, a minimum intervention in the existing concept is desirable. This is why we developed an effective upgrade of the existing concept by introducing a specialized group of intelligent electronic devices supported by a principal component analysis technique. This group should be operated alongside the existing solution to monitor the actual frequency conditions and to take over power-balancing when fine-tuning is required. This supports the existing load-shedding and improves the process of frequency stabilization.

Index Terms
Adaptive protection, demand side response, intelligent monitoring, load shedding, machine learning, power system frequency stability, power system protection.

I. Introduction

The electric power system (EPS) is one of the largest man-made artificial systems on the planet. It enables a quality of life that was never before available to the humankind. Since electrical energy is an integral part of our daily lives, any long blackouts have major negative social and economic impacts [1]. Therefore, power engineers are constantly striving towards improving the EPS performance. To mitigate the consequences of EPS malfunctions and most severe incidents, System Integrity Protection Schemes (SIPS) are implemented. One of the protective measures associated with SIPS is ensuring the frequency stability of EPS using under-frequency load-shedding (UFLS) [2]. The main objective of UFLS is to restore the balance between the generated and the consumed active power after a major deficit takes place. This is achieved by temporarily limiting the supply of electric energy to consumers.

After many years of use, we are able to recognize both the positive and the negative features of the existing (conventional/static) UFLS. The positive features are reliability, robustness and speed, while rigidness and inadaptability are negative. An analysis of past events revealed that the existing UFLS tactic is often not capable of handling the power imbalance with satisfactory precision, since its settings are static [3]. These are periodically checked and modified against potential changes in the network (on a yearly basis or even longer), but this does not take into account the variations in operating conditions in a day, a week or a season. These variations are becoming more evident, mostly due to the developments and dynamics of electricity markets and the increased penetration of intermittent renewable energy sources. Therefore, certain measures have to be taken to modify the static UFLS concept in order to successfully accommodate the new uncertainties. Our suggestion is adding a dynamic UFLS stage, which is described in detail below.

A. Review of existing concepts

A comprehensive review of state-of-the-art UFLS is [4], which is recognized as a very important contribution to UFLS from the aspect of literature classification. After thoroughly studying [4], which we used as our main guideline, we were able to narrow down the vast number of existing UFLS approaches. This resulted in no more than three groups of principles for tackling the problem of poor adaptability.

The *first* group of principles includes increasing the number of static UFLS stages, which is only effective up to a certain point. The cause for this is that static UFLS stages might begin to overlap due to (inherent or intentional) time delays. Regulations usually limit the number of static UFLS stages for this very reason (e.g. [2]), so it is hard to find schemes with

This work was funded by the Slovenian Research Agency through the research program Electric Power Systems No. P2-0356, the funding mechanism for young researchers and project Resource management for low latency reliable communications in smart grids - LoLaG, J2-9232.

The authors are with the Faculty of Electrical Engineering, University of Ljubljana, Ljubljana 1000, Slovenia (e-mail: tadej.skrjanc@fe.uni-lj.si; rafael.mihalic@fe.uni-lj.si; urban.rudez@fe.uni-lj.si).

more than ten stages in practice [5]. Additionally, an upgrade like this would require a long re-parametrization of the overall set of relays.

The *second* group of principles involves the use of wide-area monitoring system (WAMS), which provides a valuable amount of information for better decision-making. Advanced approaches were created to determine the amount of load shedding: taking advantage of the swing equation [6, 7], a system frequency response model (SFR) [8], power-flow tracking [9], the artificial neural network [10], fuzzy logic [11] and decision trees [12]. It also offers more possibilities to distribute the required load-shedding quantities among substations. For this task, [7] utilizes a mixed integer linear programming optimization technique, taking into account load availability and compensation prices offered by customers. The method in [13] calculates the wide-area index from the recorded voltage and reactive power data, whereas [9] considers the distribution factor and the priority of the loads. On the other hand, [10] makes decisions based on the electrical distances to the fault. The authors in [14] took a different approach: they used a voltage threshold in addition to the pre-set frequency threshold for UFLS activation. [15] checks if the EPS trajectory violates the stability boundary defined in the frequency versus the rate-of-change-of-frequency (*ROCOF*) phase plane, while [6] monitors the predicted frequency nadir against a minimum frequency threshold. Decisions are taken in a centralized location, which means that there is a risk of failure in the communication network to deliver accurate data in time.

The *third* principle is based on a thorough and often mathematically complex modification of the entire UFLS involving numerous under-frequency relays across the EPS. [16] proposes a decentralized multi-agent system based UFLS, where each agent shares the information about the difference between the generated and the consumed active power with neighbouring agents. They achieve consensus using the average consensus theorem and additionally use a particle swarm optimization algorithm to optimize the coefficients for information exchange. [17] uses a voltage deviation of load buses to determine the frequency threshold of each UFLS relay, whereas [18] proposes the continuous UFLS scheme to shed loads in proportion to the frequency deviation. [18] and [19] both suggest that analytical proof for UFLS scheme efficiency is required. However in this paper, we decided to use an extensive amount of case studies instead. One of the reasons for this decision is that we wanted to take into account complex dynamics of the EPS, which is usually neglected in similar analytical proofs. Authors in [20] estimate the frequency evolution in each relay by fitting the 2nd order polynomial and adjusting the frequency thresholds according to the estimated frequency nadir. The methods listed are mostly problematic from the financial point of view and due to potentially poor transparency.

It is also possible to formulate the conventional UFLS setting as an optimization problem for different EPS operating points. Solving the optimization problem (minimization/maximization of an objective function) provides the setting of conventional UFLS stages that gives the best results in average, e.g. on a yearly basis (corresponding to a global optimum of an objective function) [21-27]. However in terms of UFLS, this does not assure 100% efficiency, since it is always possible to pinpoint certain conditions in which conventional UFLS operates ineffectively, despite the optimization.

B. Paper contributions

The idea originates from the fact that the conventional UFLS is the most straightforward and the most commonly implemented UFLS scheme in use. It was proven as robust and reliable many times in the past. However, its inflexibility is also undisputable. This is why the aim of this paper was to find a cost-effective UFLS solution that involves state-of-the-art intelligent electronic devices (IED) and machine-learning technologies on one hand and keeps the positive features of conventional UFLS on the other. We especially took into consideration that several existing frequency relays in many EPSs still have older designs.

Therefore, the *first* scientific contribution of this paper is a novel and less intrusive UFLS method (from the implementation point of view) that supplements conventional UFLS by applying state-of-the-art IED and machine-learning technologies. IEDs operate alongside conventional UFLS relays and take action only when their machine-learning algorithm recognizes the need to do so. Therefore, IEDs act as an added dynamic UFLS stage, whereas the static UFLS remains unchanged. The *second* scientific contribution is a four-step algorithm for advanced operation of modern IEDs in UFLS. The algorithm provides the IEDs with a high level of situational awareness based purely on locally obtained information/measurements. The *third* contribution relates to an innovative use of the SFR model in the algorithm, i.e. for the real-time estimation of the forthcoming frequency in IEDs and self-adjustment of its triggering parameters. Furthermore, consumers taking part in such a dynamic stage could be included in a demand-side response program [7, 14] supported by appropriate contracts. The other option would be simply to choose the feeders from the existing load priority lists, as is usually the case in conventional UFLS philosophy.

II. Methodology

The conceptual role of the dynamic UFLS stage inspired the authors to name it the *libero UFLS stage* (L-UFLS). The term *libero* is used in volleyball jargon for a free defender, a player that is specialized in defensive skills but is still only one of six players on the field (an analogy to static UFLS).

As previously explained in Section I., each IED involved in L-UFLS is equipped with a novel algorithm, which is running online. The algorithm is performed in four steps (see Fig. 1). In the *first step*, real-time frequency measurements are processed

with a pattern-recognition procedure (machine learning technique) in order to establish which frequency-related conditions are present at that particular point in time. This way, IED is able to distinguish between several most characteristic frequency-related conditions in real-time. In the *second step*, we feed the same set of measurements into a fitting process. Its task is to select the parameters of a system frequency response (SFR) model [28], so that the SFR response tightly corresponds to the input measurements. This way, we are able to obtain an estimate of the forthcoming frequency trajectory when no UFLS is expected to intervene. It is important to note that the prediction error increases when observing the frequency trajectory further down the timeline, but it is within acceptable limits when we are interested in conditions a couple of seconds in advance (see Section II.C.). This is why in the *third step*, a frequency-trajectory forecast is used to establish the expected time *DT* and the frequency *DF* margins for the individual forthcoming static UFLS stages. Both margins are combined into a "take-off characteristic", providing final information on whether the static UFLS already handled most of the power imbalance. If it did, L-UFLS is set to intervene and fine-tune the power balance in the *fourth step* by modifying its frequency thresholds.

A. Achieving situational awareness by machine learning

In order to expect a sound and reasonable action from an IED, it must first be introduced to a satisfactory level of situational awareness. Since we are referring to frequency-related conditions, it is best to examine a possibility for detecting a power-imbalance incident as a main event.

The literature contains several approaches for the detection of an initial frequency drop. They can be sorted into several categories, using: *i*) fixed frequency threshold [29], *ii*) frequency change and accumulation of frequency change over time [7], *iii*) average energy of the measured frequency signal calculated from the fast Fourier transform (FFT) analysis [30], *iv*) *ROCOF* [31] and *v*) machine-learning techniques [32]. All but the latter detect the initializing incident when a certain variable violates a pre-set threshold. Since incidents that cause a frequency drop have different characteristics and sizes, such approaches are often insufficient for efficient detection [30, 32]. This is why we focused on (unsupervised) machine-learning techniques, more specifically on principal component analysis (PCA) [33]. PCA has proven to be a suitable recognition method in many fields, such as image processing, pattern recognition, classification and anomaly detection [34, 35].

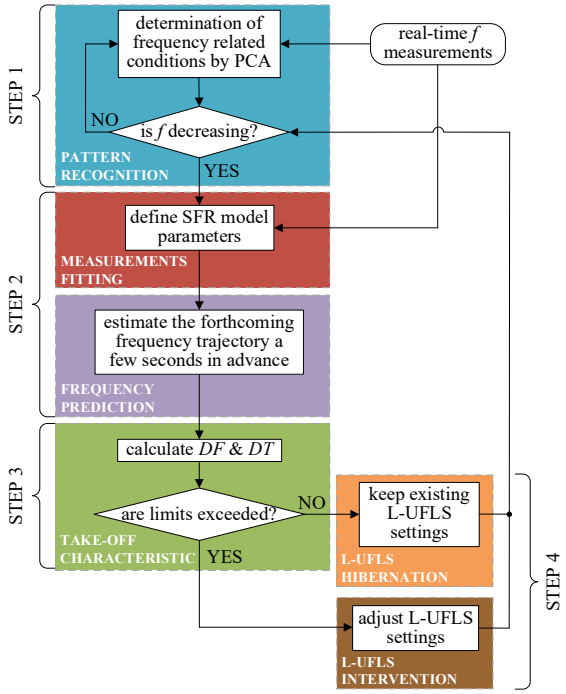

Fig. 1. Flowchart of the proposed UFLS algorithm

PCA [34, 35] is a statistical machine-learning tool that uses an orthogonal transformation to convert *m* sets of observations $\mathbf{X} = [X_1 \ldots X_m]$ described by *n* variables $\mathbf{X_i} = [x_1 \ldots x_n]$ into a new, smaller linear-space $\tilde{\mathbf{X}}_\mathbf{i} = [\tilde{x}_1 \ldots \tilde{x}_n]$ – the principal subspace (grey area in Fig. 2). The transformation is performed in such a way that the orthogonal projection of the original data points (grey blank dots in Fig. 2) onto the principal subspace minimizes the sum of squared error of the projections (e.g. distances between the original and transformed data points indicated with the grey line in Fig. 2). $\bar{\mathbf{X}}$ in Fig. 2 represents the mean value of the transformed data and vectors $\mathbf{u_1}$ and $\mathbf{u_2}$ the first two principal components. Thus, PCA decomposes the observation matrix $\mathbf{X}$ into a score matrix $\mathbf{T}$ and a loading matrix $\mathbf{P}$:

$$\mathbf{X} = \mathbf{T} \cdot \mathbf{P}^{\mathrm{T}} + \mathbf{E} = \mathbf{t}_1 \cdot \mathbf{p}_1^{\mathrm{T}} + \ldots + \mathbf{t}_j \cdot \mathbf{p}_j^{\mathrm{T}} + \mathbf{E}\,, \qquad (1)$$

where $\mathbf{t}_i$ are score vectors, $\mathbf{p}_i$ are loading vectors, $\mathbf{E}$ is the residual matrix and *j* the number of principal components.

In a principal subspace, similar observations (in our case, frequency-related patterns representing an input to PCA) form a dense cluster of points (*k*). If real-time frequency measurements $\mathbf{X_{meas}}$ are transformed into the same subspace, similarities to

any previously known conditions (output of PCA) can be found by using any distance metric classification algorithm (e.g. k-nearest neighbours, Euclidean, Cityblock, Cosine, etc.). Therefore, the performance of PCA-based pattern recognition depends on the quality of the pre-existing database used as a reference frame for comparison. This is why a database should include a large dataset of several frequency recordings captured during the pursued incidents and conditions. To obtain these, we ran numerous offline dynamic simulations. It should be kept in mind that there is no reservation against supplementing the database with real measurements.

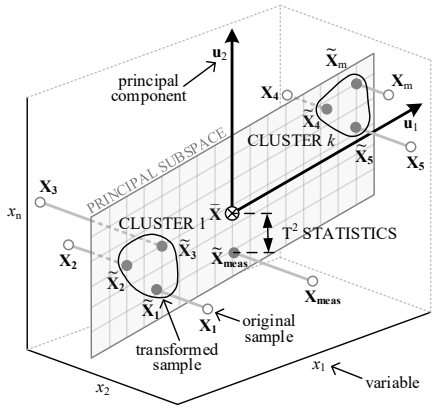

Fig. 2. A graphical representation of a PCA transformation principle

Fig. 3a depicts an example of an EPS frequency response after the occurrence of two sequential power-imbalance incidents, both within 10 seconds (simulation time t = 4.80 sec and t = 13.60 sec). A closer look reveals that a conventional UFLS was triggered six times (twice after the first incident and four times after the second incident) before the frequency was finally stabilized. Along the resulting frequency trajectory, eight characteristic patterns that were included in the database are labelled with numbers from 1 to 8. There is a prerequisite for the IED to monitor the frequency in terms of a sliding window and the following question quickly appears: What window length is the most appropriate for our purposes? To provide the answer, we must take into account the following facts: *i*) IEDs are installed in individual substations where the measured frequency is subjected to local oscillations [36], *ii*) frequency measurements contain a certain amount of noise [37] and *iii*) the duration of different dynamic phenomena in the frequency measurements might vary significantly [37]. To approach the reality, we added a Gaussian noise to the simulated frequency – see Fig. 4. A comparison to PMU measurements from a real EPS confirms that the added noise is adequate.

Our analysis stressed the limitations for the sliding window. It should be narrow enough to detect rapid frequency changes on one hand and wide enough to not be affected by electromechanical oscillations and measurement noise on the other. It became apparent that in order to satisfy these conditions, more than one sliding window should be used, with each of them having a different length.

Fig. 3b and Fig. 3c show a typical testing of the PCA recognition algorithm, with and without measurement noise in the input frequency data, respectively. The black dots represent recognition results with a 0.5 sec sliding window and grey dots represent recognition results with a 3 sec sliding window. The grey lines in the background indicate the actual frequency trend and appear useful for a first-glance orientation. The results show that by using a narrower window, the detection algorithm correctly distinguishes between all frequency patterns when there is no noise in the input signal. However if noise is present, size of the sliding window becomes more important. We will for example first focus on a 0–4.80 sec period. A wide-window algorithm correctly detects pattern 1 (steady-state), whereas the narrow-window algorithm erroneously recognizes the situation as either pattern 2 (power imbalance), pattern 3 (frequency decreasing) or pattern 7 (frequency increasing). The downside is that a wider window delays recognition, which is evident when the second power imbalance occurs. A wider window detects the second change in a main trend (transition from pattern 7 to pattern 3) 180 msec later than the narrower window. As expected, a wider window appears more appropriate for main frequency trend monitoring, whereas a narrow window is able to detect individual events (such as pattern 2). It is therefore necessary to combine recognition results from both windows in order to overcome noisy environmental conditions and eliminate false classifications, while at the same time maintaining a sufficiently high recognition speed. For instance, if a narrow window categorises an event as a power imbalance and the wider window categorises it as steady-state, it is reasonable to trust the wide-window classification.

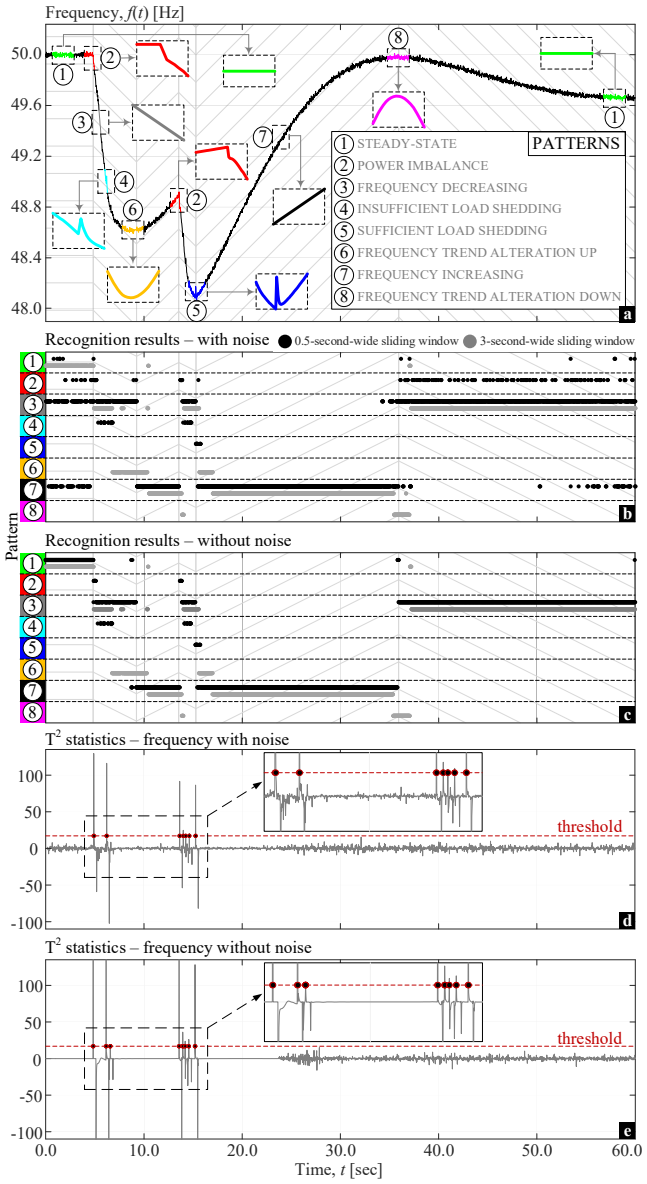

Fig. 3. EPS frequency-response patterns used during recognition process (a), recognition results considering individual sliding-window lengths (b, c) and T^2 statistic (d, e)

To further increase the recognition algorithm robustness, we have applied Hotelling's T^2 statistic, which is often utilised for disturbance identification [38]. The T^2 statistic is a scaled, squared 2-norm of an original sample from its mean value, as shown in Fig. 2. It is calculated as follows:

$$T_i^2 = \mathbf{t}_i \cdot \mathbf{\Lambda}^{-1} \cdot \mathbf{t}_i^T = \mathbf{x}_i \cdot \mathbf{P} \cdot \mathbf{\Lambda}^{-1} \cdot \mathbf{P}^T \cdot \mathbf{x}_i^T , \quad (2)$$

where $\mathbf{t}_i$ is the *i*-th row of the *j* score vectors from the PCA model, and $\mathbf{\Lambda}^{-1}$ is a diagonal matrix containing the *j* eigenvalues. Fig. 3d and Fig. 3e show the T^2 statistics for the selected case, with and without the noise in the input frequency measurements. Extreme values in both graphs indicate power imbalance and load shedding. To accurately detect these two events, a fixed threshold was used, so that a balance was found between avoiding false detections and missing a detection (as for example in Fig. 3d, where the second load shedding was not detected).

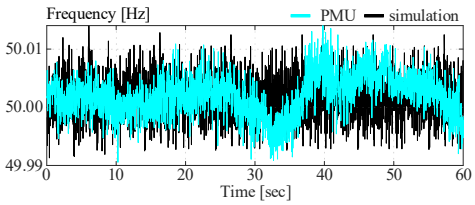

Fig. 4. Real EPS frequency measurement from two different PMUs and frequency simulation with added Gaussian noise

B. A system frequency response model

A SFR model was first introduced in [28] and was utilized in several publications since then. However, it has never been used for obtaining a short-term frequency trajectory prediction. As illustrated in Fig. 5, a SFR model consists of two main parts. The first part describes the average behaviour of the speed governors and the turbines, whereas the second part describes the

behaviour of the EPS and electrical loads. SFR was developed to average the dynamic behaviour of multiple synchronous machines into an equivalent single-generator unit model. It filters out all inter-generator oscillations and provides the average EPS response.

The purpose of a fitting process of the input frequency measurements $f(t)$ to SFR $f_{SFR}(t)$ was to estimate the unknown parameters of the SFR using the least-squares method:

$$\min \sum_{k=t_{start}}^{t_{end}} \left(f(t) - f_{SFR}(t) \right)^2 . \quad (3)$$

The fitting is initiated only after the power imbalance is detected, which defines the moment denoted by $t = t_{start}$. Denotation $t = t_{end}$ on the other hand refers to the last available real-time measurement (see Fig. 6). Mathematical rules dictate that in order to obtain the first fitting after the imbalance occurs, at least as many frequency measurements must be recorded as there are unknown parameters in the SFR model. To ensure that a fit is always possible, limit values have to be imposed on individual parameters.

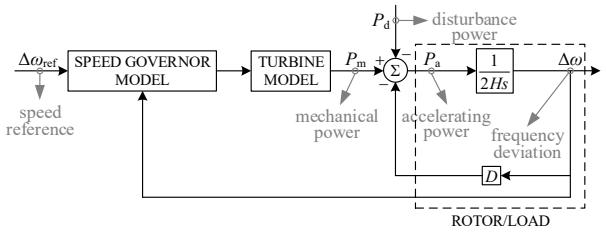

Fig. 5. A conceptual representation of a SFR model [28]

It is a fact that in various countries around the world, different electricity-generating technologies are dominant. These in turn react differently to power imbalances due to the underlying technological processes. Several different SFR models exist in the literature and a thorough analysis had to be made prior to selecting one of them in our algorithm. This is why we describe seven different SFR models, which are mathematically limited with polynomials up to the third order, mainly for two reasons: *i*) to decrease computational effort and *ii*) to capture the main frequency trend.

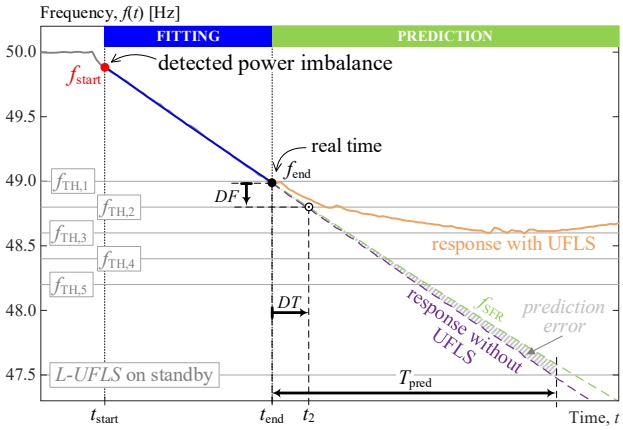

Fig. 6. Frequency prediction and time difference estimation

i) SFR model considering thermal power plants

One of the first SFR models found in the literature was proposed by Anderson and Mirheydar [28] in 1990. It is often used in frequency stability analysis and UFLS protection design. This model assumes the dominance of steam reheat turbines and neglects the effect of the excitation system, voltage dependence of the loads, nonlinearities of the turbine-governor model and all but the largest time constants. The frequency response $\Delta\omega$ is [28]:

$$\Delta\omega(s) = \frac{RP_d(T_R s + 1)}{(2HRT_R)s^2 + (2HR + DRT_R + K_m F_H T_R)s + (DR + K_m)}, \quad (4)$$

where R stands for governor control, P_d disturbance power in p.u., D damping factor, H inertia constant in sec, K_m mechanical power gain factor, F_H fraction of the total power generated by the turbine and T_R reheat time constant in sec.

ii) SFR model considering hydro power plants

In many countries, a large part of electricity is supplied by hydro power plants. To represent their response, we use the linearized IEEEG3 model that adopts a linear turbine model [39]. Its frequency response can be calculated as follows:

$$\Delta\omega(s) = \frac{\frac{1}{2Hs+D}}{1 + \left(\frac{1}{2Hs+D}\right)\left(\frac{(1+T_R s)\cdot(1-T_W s)}{(1+T_G s)\cdot(1+(R_T/R_P)T_R s)\cdot(1+0.5T_W s)\cdot R_P}\right)}, \quad (5)$$

where R_T is temporary droop, R_P permanent droop, T_W water inertia time constant, T_R dashpot time constant and T_G main servo time constant.

iii) General SFR model

In reality, we usually deal with a combination of several different types of power plants. Therefore, the simultaneous presence of various electricity sources was analysed and suggested by the authors in [40] in the form of a turbine-governor transfer function:

$$G_{\mathrm{m}}(s)=\frac{\Delta P_{\mathrm{m}}}{\Delta f}=\left(\sum_{j=1}^{J} b_{\mathrm{j}} s^{J-j} \Big/ \sum_{i=1}^{I} a_{\mathrm{i}} s^{I-i}\right),\ a_{\mathrm{1}}=1,\ J=I-1, \quad (6)$$

where a_{i} and b_{j} are the coefficients of the transfer function. The frequency response Δf is then calculated as follows:

$$\Delta f(s)=\frac{P_{\mathrm{d}}}{(2Hs+K_{\mathrm{D}})+G_{\mathrm{m}}(s)},\ K_{\mathrm{D}}=D+K_{\mathrm{L}}, \quad (7)$$

where K_{L} is the frequency coefficient of the load. The value I determines the transfer function order and was varied from 1 to 3 (used as index in the continuation).

iv) A 3rd order EPS transfer function

Inspired by the previous model, we constructed a similar transfer function. Its order in the nominator equals the order in the denominator:

$$\Delta f(s)=P_{\mathrm{d}}\cdot\left(\sum_{i=1}^{3} a_{\mathrm{i}} s^{i} \Big/ \sum_{j=1}^{3} b_{\mathrm{j}} s^{j}\right), \quad (8)$$

where a_{i} and b_{j} are the coefficients of the transfer function.

v) Estimation of the frequency-response

The EPS frequency response in the time domain depends on the number and the type of poles of the transfer function used for the representation of the average network behaviour [41]. According to this, we are able to estimate/guess the response. We assume a real and complex conjugated pair of poles, resulting in the following time-domain response:

$$\Delta\omega(t)=A+B\cdot e^{C\cdot t}+D\cdot e^{E\cdot t}\cdot\cos(F\cdot t+G), \quad (9)$$

where A, B, C, D, E, F and G are the adjustment parameters.

C. Forecasting the forthcoming frequency-trajectory and a prediction error analysis

A satisfactory fit of the selected SFR model with frequency measurements enables us to forecast the forthcoming frequency trajectory when no UFLS activation is expected. To verify the forecast accuracy with different SFR models described in Section II.B., we compare the estimated frequency trajectory f_{SFR} with the actual frequency trajectory f obtained by the dynamic simulation. The prediction error *ERR* was observed by varying the prediction time horizon (T_{pred} = 1 sec, 5 sec and 10 sec, respectively) – see Fig. 6:

$$ERR=f_{\mathrm{SFR}}(T_{\mathrm{pred}})-f(T_{\mathrm{pred}})\cdot \quad (10)$$

In Fig. 6, the power imbalance invokes the frequency drop, which is detected at $t = t_{\mathrm{start}}$. The static UFLS thresholds $f_{\mathrm{TH,i}}$ are distributed among 48.0 and 49.0 Hz and inactive, whereas dynamic L-UFLS hibernates at the frequency-stability limit of 47.5 Hz. The forthcoming frequency-trajectory is predicted at $t = t_{\mathrm{end}}$ and there is a clear mismatch between the *actual* future frequency trajectory (dashed purple curve) and the *predicted* one (dashed green curve). The boxplot in Fig. 7 summarizes the results, where the SFR fitting was performed by taking into account the SFR parameter constraints in TABLE I. The analysis included the prediction error of individual SFR models for numerous cases that differ in network topology, power plant types and governors.

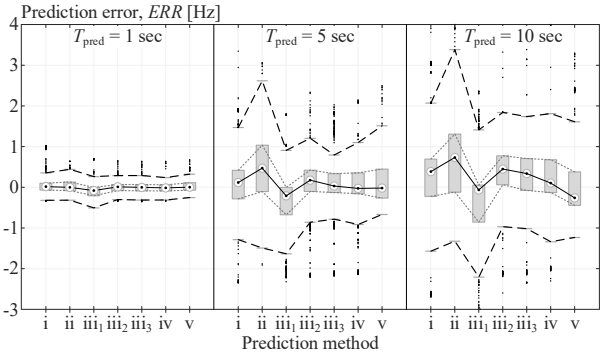

Fig. 7. Frequency prediction error *ERR* of different SFR models with a variable prediction time horizon T_{pred}

Negative/positive error values in Fig. 7 mean that the prediction assumed a more or less severe frequency drop when compared to the actual conditions. Fig. 7 shows that the greater the prediction time T_{pred} is, the greater the prediction error *ERR* is. The average error ranges from –80.1 mHz to +16.9 mHz for T_{pred} = 1 sec, from –210.2 mHz to +470.1 mHz for T_{pred} = 5 sec and from –259.8 mHz to +733.1 mHz for T_{pred} = 10 sec. Most of the outliers (black dots in Fig. 7) originate from the first few frequency estimates when the number of frequency samples is scarce and the IED finds it extremely difficult to calculate the electrical frequency due to underlying transients.

TABLE I
PARAMETER CONSTRAINTS OF DIFFERENT SFR MODELS USED DURING THE FITTING PROCESS

SFR MODEL		PARAMETER CONSTRAINTS								
i		P_d	H	D	R	K_m	F_H	T_R		
	min	-0.5	3	0	0.03	0.8	0.1	4		
	max	0.0	20	8	0.60	1.2	0.4	14		
ii		P_d	H	D	R_T	R_P	T_W	T_R	T_G	
	min	-0.5	3	0	0.3	0.01	0	2.5	0.001	
	max	0.0	20	8	20.0	0.30	5	25.0	1.000	
iii_1		P_d	H	K_D	a_0	a_1	a_2	b_0	b_1	b_2
	min	-0.5	3	4	10	/	/	3	/	/
	max	0.0	20	15	50	/	/	190	/	/
iii_2		P_d	H	K_D	a_0	a_1	a_2	b_0	b_1	b_2
	min	-0.5	3	3	50	20	/	100	3	/
	max	0.0	20	15	300	50	/	200	20	/
iii_3		P_d	H	K_D	a_0	a_1	a_2	b_0	b_1	b_2
	min	-0.5	3	4	0	60	15	0	20	5
	max	0.0	20	15	100	150	60	100	100	15
iv		P_d	a_0	a_1	a_2	a_3	b_0	b_1	b_2	b_3
	min	-0.5	0	0	0	0.9	0	0	0	0.9
	max	0.0	100	100	100	1.1	100	100	100	1.1
v		A	B	C	D	E	F	G		
	min	0.00	0.00	-1	0.00	-0.30	0.0	-1		
	max	0.01	0.08	0	0.08	-0.03	0.2	2		

D. Setting-up a take-off characteristic

Once the forthcoming frequency-trajectory is available with no UFLS intervention accounted for, IED is able to observe the remaining time *DT* before each (*i*-th) forthcoming static UFLS threshold $f_{TH,i}$ is expected to be reached (see Fig. 6, in which *DT* is depicted for index $i = 2$) as follows:

$$DT = t_i - t_{end},\ i = 1...N_{UFLS}, \quad (11)$$

where t_i is the time of the expected breach of the static UFLS stage, t_{end} is the real time and N_{UFLS} indicates the overall number of static UFLS stages. If the frequency has already passed a certain threshold or a threshold violation is not expected in the future, we assign a large default value to t_i (e.g. 50 sec). *DT* provides us with important but still insufficient time-related information. An identical *DT* can namely indicate different alarming situations, depending on the frequency at that particular instant f_{end}. This is why the remaining frequency margin until the *i*-th forthcoming static UFLS threshold is needed as well:

$$DF = f_{end} - f_{TH,i}. \quad (12)$$

It is possible to argue that dealing with *DT* and *DF* at the same time could be replaced by *ROCOF*. This is why we have to stress that by using *ROCOF* for prediction purposes, you would assume a future frequency decay of constant rate, whereas the described process takes into account the potential influence of all control mechanisms (e.g. governor action, impact of loads). This is an important contribution resulting in less tripping and an improved EPS frequency response.

The information provided individually by *DF* and *DT* can be merged into a *DF-DT* plane, in which IED is able to monitor the severity of frequency conditions in real time. An example of the *DF-DT* plane in which the *take-off characteristic* is marked with a shaded area can be found in Fig. 8b and Fig. 8c. Fig. 8a depicts EPS frequency responses with two different power imbalances (larger imbalance – red line, smaller imbalance – blue line).

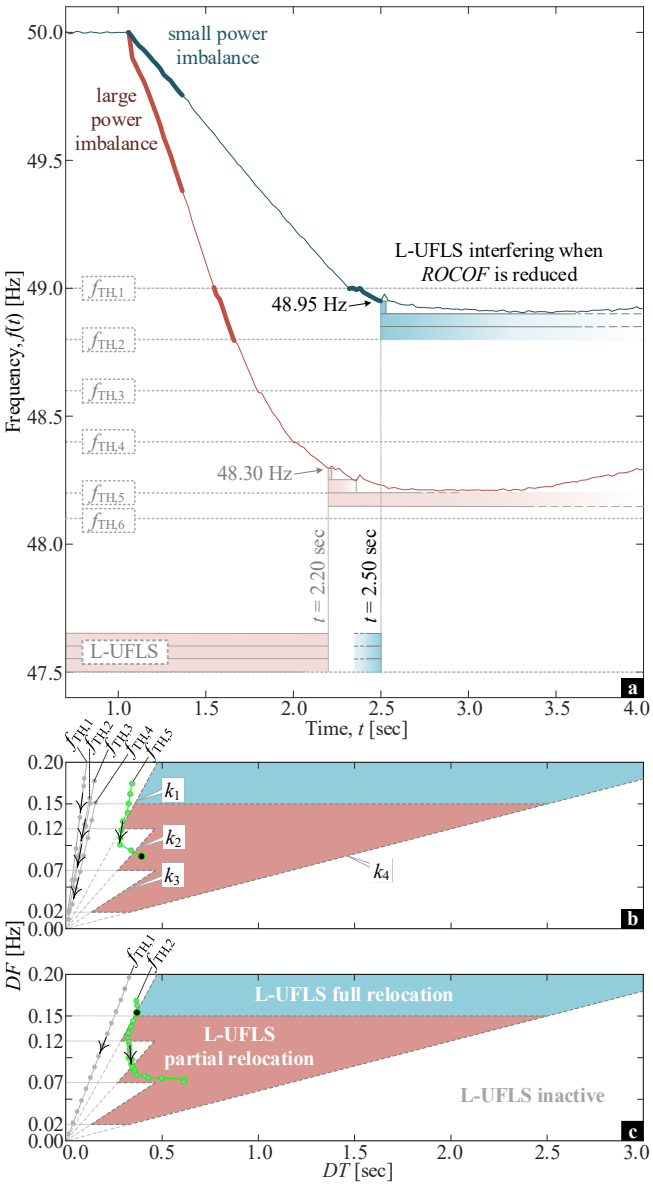

Fig. 8. An illustrative example of the L-UFLS operation (a) and a corresponding take-off characteristic for a more (b) and less (c) severe case

The conventional UFLS scheme used in this paper consists of six stages (10-10-10-10-10-5%) placed between 48.0 Hz and 49.0 Hz (0.2 Hz apart). Therefore, the vertical range of the DF-DT plane is limited to 0.2 Hz. When it comes to the number of IED devices and their locations, we accepted the limitations from regulatory requirements of ENTSO-E [2], according to which the maximum amount of system loading covered by a single static (conventional) UFLS stage should be equal to 10% of the total EPS load (in each point in time). Therefore, since we have decided to split L-UFLS into three equally distributed dynamic sub-stages placed 0.2 Hz / 4 = 0.05 Hz apart, their sum corresponds to the size of the largest static UFLS stage (i.e. 10%). To avoid overlapping between the static UFLS and L-UFLS, we had to define a minimum *DF* value that was set to 0.02 Hz. Furthermore, depending on the *DF* value when L-UFLS is activated (step 4 in Fig. 1), all three L-UFLS sub-stages do not always fit between two subsequent static frequency thresholds. The minimum *DF* value required for activating all three sub-stages equals 0.15 Hz, therefore L-UFLS sub-stages are placed at $f_{TH,i}$ + [0.02, 0.07, 0.12] Hz in such cases. On the other hand, a *DF* value of at least 0.12 is needed for activation of two sub-stages (sub-stages placed at $f_{TH,i}$ + [0.02, 0.07] Hz). For a single sub-stage, the minimum *DF* equals 0.02 Hz (L-UFLS sub-stage at $f_{TH,i}$ + 0.02 Hz). Depending on how many L-UFLS sub-stages fit between two consecutive static thresholds, we are able to handle differently-serious situations. As a result, we need three different starting constraints (denotation *j*) in the take-off characteristic (denoted by k_1 to k_3, where index 1 corresponds to all three sub-stages and index 3 to a single sub-stage). These constraints represent a constant *DF*/*DT* ratio and were set as k_1 = 0.42, k_2 = 0.26 and k_3 = 0.15 in this paper, based on experience gained by running numerous dynamic simulations. The fourth and final constraint k_4 = 0.06 in Fig. 8 represents conditions in which the frequency is expected to improve without UFLS.

After the fault causing frequency excursion, the operating point in the *DF-DT* plane begins its path along the trajectory, starting with *DF* = 0.2 Hz. In case of a fast frequency decay (Fig. 8b), the initial trajectory is located on the left side of the shaded area and is directed towards the diagram origin. This occurs when we let the conventional UFLS to act and L-UFLS

hibernates. After each static threshold is reached, the trajectory suddenly shifts from the diagram origin back towards a value of DF = 0.2 Hz, but each time closer to the shaded area. Once the trajectory reaches the take-off characteristic (after four conventional UFLS stages), L-UFLS is initiated. In case of moderate frequency decay (Fig. 8c), a single conventional UFLS suffices before L-UFLS is activated.

E. Self-adjustment of L-UFLS settings

In order to wait for frequency prediction after a power-imbalance incident occurs in the EPS, L-UFLS is initially set to hibernate below all the static UFLS thresholds. In this paper, the hibernation threshold was set to 47.5 Hz (see three red and blue rectangles at the bottom of Fig. 8a). As soon as the decreasing frequency trend is recognised by the machine-learning functionality and the take-off characteristic is violated (see the black dot in Fig. 8b and Fig. 8c), the L-UFLS automatically self-adjusts its thresholds. This is achievable in a very short period of time (in the range of IED-code execution rate), since there are no third-party elements involved, e.g. via the IEC 61850 protocol. Any modern IED offers enough hardware capabilities for this purpose. Depending on the DF value at that instant, one of the two possible adjustments is selected:

1) full relocation: if $DF \geq 0.15$ Hz (see Fig. 8c), all three sub-stages fit between two consecutive static UFLS (see a small power imbalance case in Fig. 8a and Fig. 8c, which sets the first out of three L-UFLS sub-stages to 48.95 Hz),
2) partial relocation: if 0.02 Hz $\leq DF <$ 0.15 Hz, the first of three L-UFLS sub-stages is set to the value of the real-time frequency value since not all three sub-stages fit between the two consecutive static UFLS (i.e. 48.30 Hz in the case of large power imbalance in Fig. 8a and Fig. 8b).

A very important aspect of L-UFLS is that each IED included in L-UFLS acts according to the locally measured frequency. Therefore, IED decisions and actions are not synchronised. This way, L-UFLS tripping is more time-dispersed, which results in a more continuous power re-balancing compared to any coordinated UFLS approaches.

III. Analytical model of the L-UFLS

In this section, L-UFLS efficiency is evaluated analytically using the SFR model, similar to [19].

A. Multi-machine SFR model

If one generalizes equation (4) in Section II.B.i) to N generators, we obtain [19]:

$$\Delta\omega(s) = \frac{-\Delta P_{\mathrm{d}}(s)\prod_{i=1}^{N}\left(1+sT_{\mathrm{R,i}}\right)}{(2Hs+D)\prod_{i=1}^{N}\left(1+sT_{\mathrm{R,i}}\right)+\sum_{j=1}^{N}\left[\frac{K_{\mathrm{m,j}}}{R_{\mathrm{j}}}\left(1+F_{\mathrm{H,j}}T_{\mathrm{R,j}}s\prod_{i=1,i\neq j}^{N}\left(1+sT_{\mathrm{R,i}}\right)\right)\right]}, \quad (13)$$

where the parameters have the same meaning as in (4). If a sudden imbalance between load and generation is represented as a step change $\Delta P_{\mathrm{d}}(s) = \Delta P_{\mathrm{d}}/s$, the dynamic load-frequency response after a contingency can be represented as follows [19]:

$$\Delta\omega(s) = \Delta P_{\mathrm{d}}\sum_{i=1}^{N+1}\frac{A_{\mathrm{i}}}{p_{\mathrm{i}}}\cdot\left(\frac{1}{s}-\frac{1}{s-p_{\mathrm{i}}}\right), \quad (14)$$

where A_{i} is either real or complex and p_{i} is either a root or a pole of the denominator of (13). Thus, the time response of the N+1st order SFR model is:

$$\Delta\omega(t) = \Delta P_{\mathrm{d}}\sum_{i=1}^{N+1}\frac{A_{\mathrm{i}}}{p_{\mathrm{i}}}\cdot\left(1-e^{p_{\mathrm{i}}t}\right)\cdot U(t)\,. \quad (15)$$

Equations (13)-(15) provide the analytical model of the free response of the system to the sudden imbalance contingency.

B. UFLS modelling

To include UFLS in such SFR model, we need to develop its analytic model. UFLS is defined by the number of stages $r_{\mathrm{S,max}}$, the load shedding amount ΔP_{j}, the corresponding stage threshold frequency $f_{\mathrm{TH,j}}$ and time delay t_{dj}, where index j = 1,… $r_{\mathrm{S,max}}$ represents the individual load shedding stage. The total amount of load shedding P_{LS} can be expressed as the sum of incremental step functions [19]:

$$P_{\mathrm{LS}}(s) = \sum_{j=0}^{M}\frac{\Delta P_{\mathrm{j}}}{s}\cdot e^{-\tau_{\mathrm{j}}s},\ 0\leq M\leq r_{\mathrm{S,max}},\ \tau_0 = 0\ , \quad (16)$$

$$P_{\mathrm{LS}}(t) = \sum_{j=0}^{M}\Delta P_{\mathrm{j}}\cdot U(t-\tau_{\mathrm{j}})\ , \quad (17)$$

where τ_{j} is the moment of the j-th load shedding stage activation, M is the actual number of activated conventional load shedding stages and ΔP_0 is the initial power imbalance between load and generation.

C. SFR-L-UFLS model

If we want to include expression (16) in the multi-machine SFR model (14), we need to replace ΔP_{d} in (14) by $P_{\mathrm{LS,}}$ expressed by (16). As a result, the SFR-L-UFLS model can be written as:

$$\Delta\omega(s) = \sum_{j=0}^{M}\frac{\Delta P_{\mathrm{j}}}{s}\cdot e^{-\tau_{\mathrm{j}}s}\cdot\sum_{i=1}^{N+1}\frac{A_{\mathrm{i}}}{p_{\mathrm{i}}}\cdot\left(\frac{1}{s}-\frac{1}{s-p_{\mathrm{i}}}\right). \quad (18)$$

Compared to using the simulation model, the SFR-L-UFLS model can be used to analytically determine some basic indicators that define the system and UFLS performance [19]:

1) the frequency-time response of the EPS

$$\Delta\omega(t) = \sum_{j=0}^{M} \Delta P_{\mathrm{j}} \cdot \sum_{i=1}^{N+1} \frac{A_{\mathrm{i}}}{p_{\mathrm{i}}} \cdot \left(1 - e^{p_{\mathrm{i}}(t-\tau_{\mathrm{j}})}\right) \cdot U\left(t - \tau_{\mathrm{j}}\right), \tag{19}$$

2) *ROCOF*

$$\frac{d\Delta\omega(t)}{dt} = -\sum_{j=0}^{M} \Delta P_{\mathrm{j}} \cdot \sum_{i=1}^{N+1} A_{\mathrm{i}} \cdot e^{p_{\mathrm{i}}(t-\tau_{\mathrm{j}})} \cdot U\left(t - \tau_{\mathrm{j}}\right), \tag{20}$$

3) steady-state frequency deviation

$$\Delta\omega_{\mathrm{ss}} = \lim_{t\to\infty} \Delta\omega(t) = \sum_{j=0}^{M} \Delta P_{\mathrm{j}} \cdot \left(\sum_{i=1}^{N+1} \frac{A_{\mathrm{i}}}{p_{\mathrm{i}}}\right), \tag{21}$$

4) minimum transient frequency deviation

$$0 = -\sum_{j=0}^{M} \Delta P_{\mathrm{j}} \cdot \sum_{i=1}^{N+1} A_{\mathrm{i}} \cdot e^{p_{\mathrm{i}}(t_{\min}-\tau_{\mathrm{j}})} \cdot U\left(t - \tau_{\mathrm{j}}\right), \tag{22}$$

5) timing and number of load shedding stages

$$\Delta\omega_{\mathrm{TH},(\mathrm{r}+1)} = -\sum_{j=0}^{r} \Delta P_{\mathrm{j}} \cdot \sum_{i=1}^{N+1} \frac{A_{\mathrm{i}}}{p_{\mathrm{i}}} \cdot \left(1 - e^{p_{\mathrm{i}}(\tau'_{\mathrm{r}+1}-\tau_{\mathrm{j}})}\right) \cdot U\left(t - \tau_{\mathrm{j}}\right), \tag{23}$$

6) take-off characteristic

$$\frac{DF}{DT} = \frac{\left(1 + \Delta\omega(t)\right) \cdot f_{\mathrm{rated}} - f_{\mathrm{TH},(\mathrm{rS}+1)}}{\tau'_{\mathrm{rS}} - t} \le k_{\mathrm{l}},\ l = 1...3\,. \tag{24}$$

These six performance indicators can be obtained by an iterative procedure, depicted in Fig. 9. The purpose of Fig. 9 process is to determine all the load shedding interventions and their effects on the frequency response. Since L-UFLS is intended to complement conventional UFLS, the process in Fig. 9 is divided into two parts (see green and orange shaded areas). First, we initialize the counters for the conventional (r_{S}) and L-UFLS (r_{L}) stages as well as f_{TH}. After that, we observe the onset time $t_{\min}$ and the value $f_{\min}$ of the minimum frequency, assuming that no UFLS stage is activated (see (22) and (19)). If $f_{\min}$ is smaller than f_{TH}, apparently f_{TH} is about to be violated. Indication of *DF/DT* (see (24), where we assume that the frequency prediction error equals 0 and f_{rated} is the nominal frequency) being larger than k_{l} invokes the L-UFLS hibernation by increasing the counter r_{S} and calculating the activation time of the first conventional UFLS stage τ'_{rS} (23). This process is repeated until either all conventional stages are activated ($r_{\mathrm{S}} = r_{\mathrm{S,max}}$) or *DF/DT* is less than k_{l}. This is the starting point of L-UFLS activation. When *DF/DT* is smaller than k_{l}, the algorithm is forced to decide on L-UFLS relocations (either partial or full, depending on the situation, see Section II.E.). For each L-UFLS activation (denotation L represents the actual number of activated L-UFLS sub-stages), the corresponding activation times τ'_{rL} are determined, which initiates another iteration.

D. Performance comparison to conventional UFLS

Using the SFR-L-UFLS model from Section III.C. and the algorithm shown in Fig. 9, we can analytically evaluate the effectiveness of L-UFLS. An example of such an evaluation is provided in Fig. 10, which shows a comparison of the frequency response (Fig. 10a) and total load shedding amount (Fig. 10b) of 6-stage conventional UFLS (grey line) and L-UFLS (black dashed line). For the purpose, we used a simple 2nd order SFR model (i.e. $N = 1$) by Anderson [28] with the following settings: $\Delta P_{\mathrm{d}} = -0.150$ pu, $H = 3.0$ sec, $R = 0.045$, $D = 0.1$, $T_{\mathrm{R,1}} = 8.5$ sec, $K_{\mathrm{m,1}} = 0.36$ and $F_{\mathrm{H,1}} = 0.2$. It can be seen that L-UFLS triggers three static stages (see red circles) and one dynamic sub-stage, since at the simulation time 2.7546 sec (see green dot) all conditions for a full L-UFLS relocation are fulfilled. Since the calculated minimum frequency considering the operation of the three static stages and one dynamic sub-stage (i.e. 48.4061 Hz) is larger than the frequency limit of the fourth static stage (i.e. 48.4000 Hz), the algorithm terminates. Thus, L-UFLS sheds 6.6% less load than conventional UFLS.

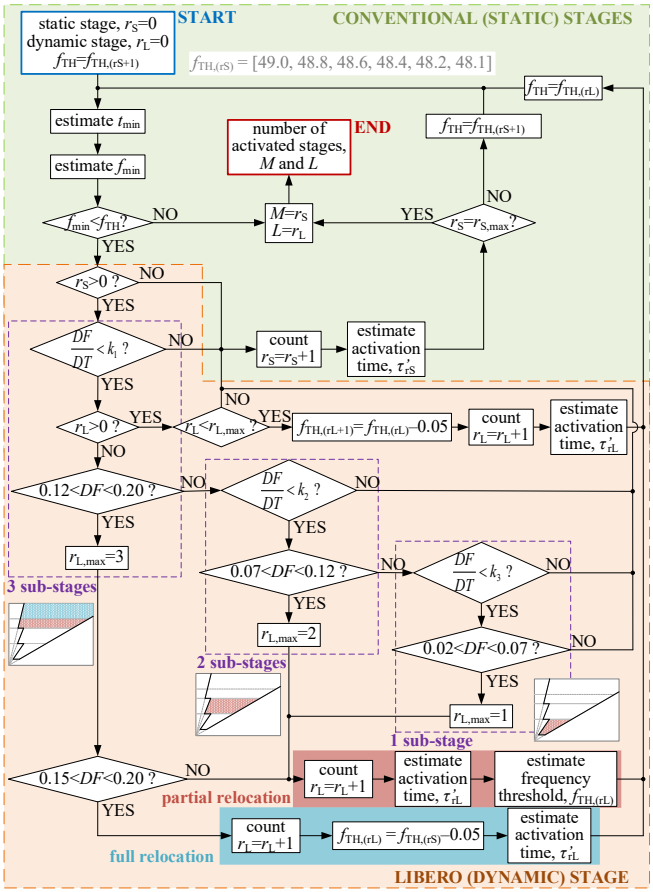

Fig. 9. Computational SFR-L-UFLS model

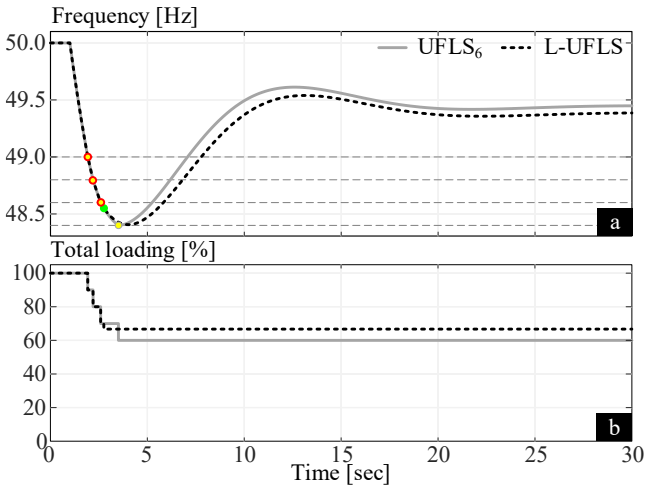

Fig. 10. Frequency response and total load shedding amount calculated by SFR-L-UFLS model

This analytical model is based on a simple SFR. For improved EPS modelling, a more complex SFR model could be used instead, describing a wider variety of power generation technologies. However, even by doing so, several aspects of the EPS dynamics would still be neglected, such as the limited spinning reserve, the inter-generator oscillations, the nonlinearities of the turbine-governor model, etc. This is why only by performing a series of off-line dynamic simulations (considering different power imbalances, different grid sizes and topologies, etc.) truly representative results about the UFLS efficiency can be obtained. Namely, ignored EPS dynamics in the analytical model indicates better L-UFLS performance than would be expected in reality. For this reason, it is reasonable to provide the test results in terms of RMS dynamic simulations in Section IV.

IV. Case studies

To test the proposed algorithm, we applied it to two EPS models of different scales, both validated against PMU recordings of past events [42]. *First*, we investigated how L-UFLS improves the frequency stabilization process in a small-size network (section IV.A.), which often attracts attention, as it experiences a transition into island operation several times a year. The L-UFLS scheme was implemented with two IEDs placed in different substations. Since three L-UFLS sub-stages are considered, each sub-stage covers 3.3% of the consumers. The PCA database has been built from 1000 dynamic simulations and frequency

recordings, which differ in terms of power mismatch, power plant types, topology and controllers. To recognise frequency-related events and calculate the T^2 statistics, 500 msec and 3000 msec sliding windows were implemented. The PCA similarity was evaluated based on the k-nearest neighbour classification algorithm and the Euclidean distance metric. For frequency estimation, we used the SFR model from Section II.B.iv) .

Second, we analysed L-UFLS impact on a large-scale network, i.e., a dynamic model of the entire Slovenian EPS (section IV. B.), the description of which can be found in [42]. Due to the size, the different voltage levels (110 kV, 220 kV and 400 kV), the variety of power plant types, the presence of a phase-shifting transformer, a STATCOM device and several other static compensation devices, we consider that it fulfils the criteria of a large-scale realistic EPS. The L-UFLS scheme was implemented by means of 15 IEDs evenly dispersed around the network. All other settings (PCA database, sliding window size, metric distance), conventional UFLS setting and the number of L-UFLS sub-stages remain the same to a small-size network.

To confirm the approach viability, it is appropriate to provide the time requirement for execution of processes that are supposed to run in the IED in real time. Using our laboratory PC with Intel® Core™ i7-7700 CPU, 3.60 GHz, 16 GB RAM, the entire IED processes required less than 20 msec (prediction 10 msec, data preparation, PCA transformation, distance computation and k-smallest distance determination up to 7 msec, estimation of the take-off characteristic 0.3 msec). It should also be emphasised that there still must be many opportunities for code optimization.

A. L-UFLS efficiency in a small-size network

We evaluated the L-UFLS efficiency in the range from 1 up to 80 MW power deficit in 1 MW increment. Fig. 11 shows the percentage of EPS de-loading by applying conventional (empty grey dots) and presented (full black dots) UFLS. The improvement is indicated by a grey-shaded area, which means that L-UFLS intervened in 42% of all cases. With L-UFLS, interrupted load is more linearly dependent on power deficit and is always less or equal than the conventional UFLS. The maximum reduction of 6.43% occurs at power deficit of 47 MW. Since regulations [2] prohibit UFLS intervention before the frequency exceeds 49.0 Hz, the L-UFLS stage is set to not modify the first stage.

A negative by-product of interrupting too much load is the resulting frequency overshoot. The upper set of circles and dots in Fig. 12 shows these overshoots for all simulated cases. In the majority of cases, L-UFLS successfully eliminates the overshoot. On the other hand, the frequency nadir (the lower set of circles and dots in Fig. 12) is slightly lower.

Since the main task of UFLS protection is to stabilize the frequency and bring the *ROCOF* value as close to zero as possible [1, 4], Fig. 13 also shows the *ROCOF* value after the last UFLS intervention. It can be seen that L-UFLS significantly reduces this value, keeping it slightly below zero in order to leave the frequency control to handle the rest.

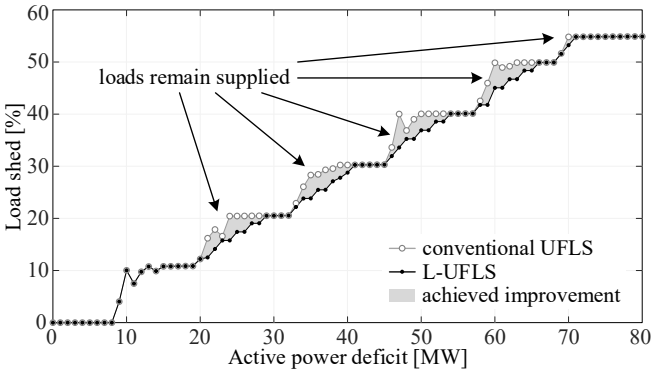

Fig. 11. Total load shedding amount of the conventional UFLS and L-UFLS (small-size network)

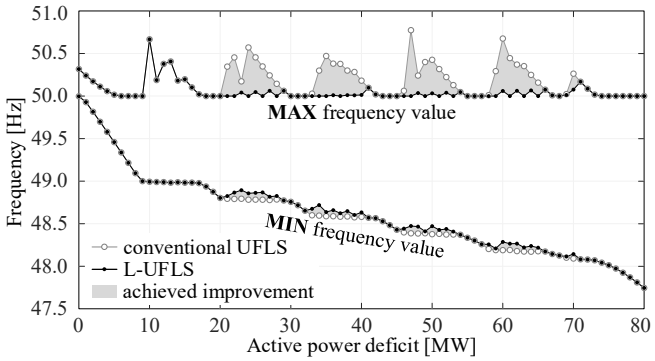

Fig. 12. Maximum and minimum frequency during the frequency transient (small-size network)

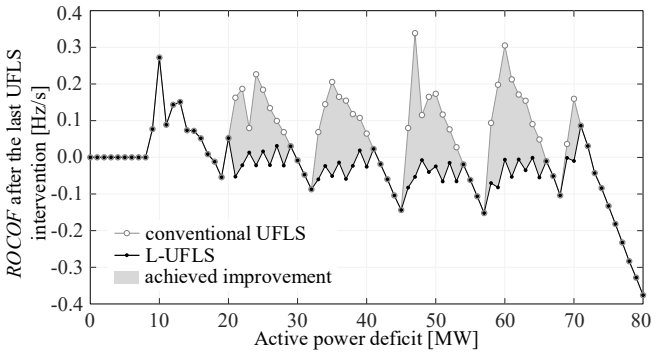

Fig. 13. *ROCOF* after the last UFLS intervention (small-size network)

B. L-UFLS efficiency in a large-size network

The L-UFLS efficiency was evaluated over a wide range of active-power deficit values, ranging from 1 MW to 1400 MW with an increment of 20 MW. Similar to Fig. 11, Fig. 14 shows the percentage of EPS de-loading when the conventional (blank grey dots) and proposed (black dots) UFLS are applied, with the improvement due to L-UFLS indicated by a grey-shaded area. However, compared to Fig. 11, Fig. 14 shows additional cases where L-UFLS is able to shed more load than the conventional UFLS, indicated by a yellow-shaded area. Once more, L-UFLS causes the amount of interrupted load to come closer to a linear relationship and is always less than or equal to the load interruption of the conventional UFLS (the maximum reduction is 5.27% for a 500 MW deficit case). A few exceptions can be seen in the yellow-shaded area on the right side, where a conventional UFLS fully exhausts a load reduction of 55%, while L-UFLS is able to stabilize more cases as it contributes 10% to the total load reduction (UFLS controls 65% instead of 55% of the system load). A comparison of Fig. 11 and Fig. 14 also reveals that the improvement by L-UFLS is more significant in a small-size network due to lower inertia.

Fig. 15 shows the corresponding maximum (overshoot) and minimum (nadir) frequencies reached during a transient in each simulated case. It can be noticed that there are no significant overshoots in the large-size network, regardless of the UFLS philosophy. The reason for this is the larger inertia value compared to a small-size network, which limits fast frequency changes.

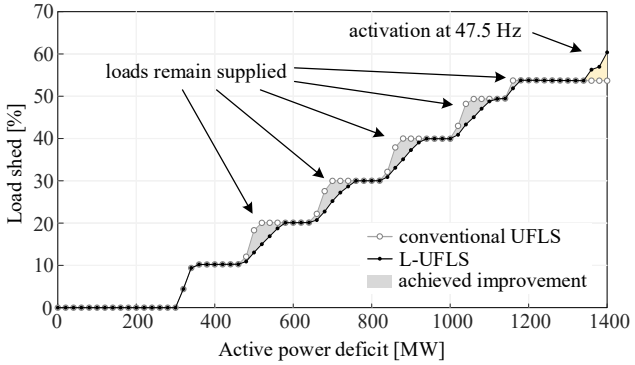

Fig. 14. Total load shedding amount of the conventional UFLS and L-UFLS (large-size network)

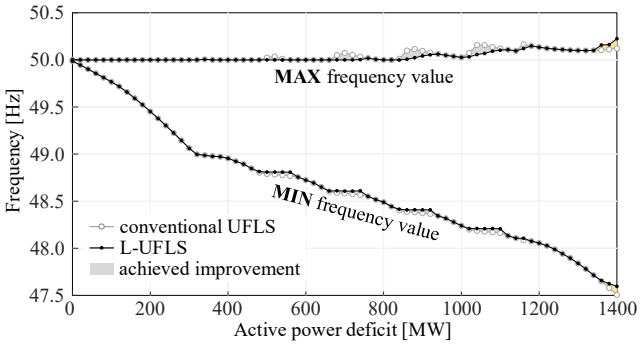

Fig. 15. Maximum and minimum frequency during the frequency transient (large-size network)

Similarly, to the case of a small-size network, Fig. 16 shows the *ROCOF* value a moment after the last UFLS intervention. Again, L-UFLS reduces this value well towards zero, giving the frequency control time to regulate the frequency.

In the final stage of the analysis, we tested how IED distribution and IED count in the system influences the efficiency of the scheme. For this purpose, we tested three different IED distributions: *i*) minimum number of IEDs located in the very vicinity of a single substation (distribution 1), *ii*) maximum number of IEDs evenly dispersed across the entire system (distribution 3) and *iii*) hybrid distribution between *i* and *ii* (distribution 2). The results in Fig. 17 indicate that frequency responses in all three scenarios are identical. The IED distribution matters only when we take into account the possibility of islanding certain

portions of the studied EPS. In this case, it makes sense to distribute the IEDs as evenly as possible throughout the EPS (a single IED for each substation).

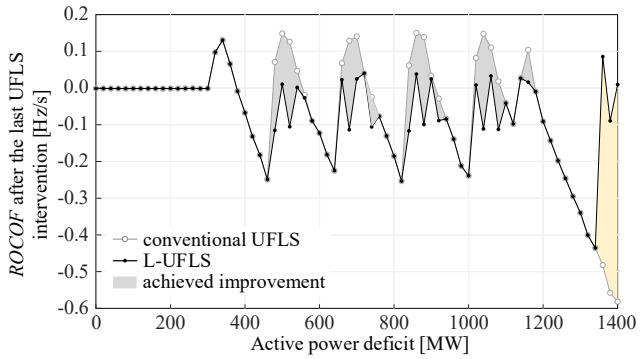

Fig. 16. *ROCOF* after the last UFLS intervention (large-size network)

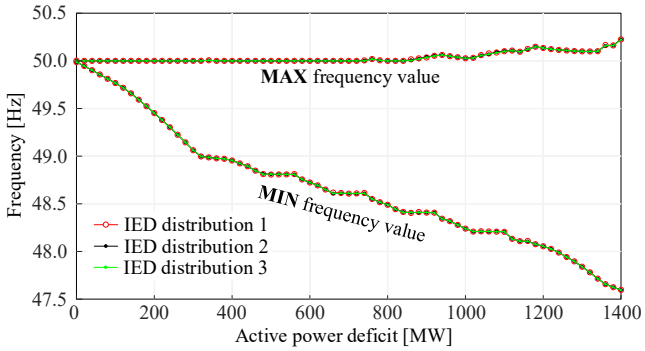

Fig. 17. Negligible impact of IED distribution in the system

C. Impact of the number of UFLS stages

In general, the number of L-UFLS sub-stages depends on the desired fine-tuning of the power imbalance. However, real IED devices need some time to respond to a trigger signal, so more sub-stages do not necessarily mean better performance, as the UFLS stages may overlap. This is why we do not recommend a large number of L-UFLS sub-stages. To show that three L-UFLS sub-stages are sufficient, we compare the L-UFLS with the 4-stage ($UFLS_4$), 6-stage ($UFLS_6$), 10-stage ($UFLS_{10}$) and 50-stage ($UFLS_{50}$) conventional UFLS. The static stages are evenly distributed between 48.0 Hz and 49.0 Hz. Among the listed conventional UFLS, the $UFLS_{50}$ achieves the most accurate active-power balance, so we use it as a reference for evaluating other UFLS schemes. Fig. 18 shows the deviation from the load shed amount of $UFLS_{50}$ as a function of the active power deficit. Therefore, a positive/negative value means a higher/lower amount of interrupted customers. As expected, $UFLS_4$ disconnects the largest amount of loads in most cases (i.e. 48.15% of all cases). Since $UFLS_4$, $UFLS_6$ and L-UFLS have the same first stage (10% at 49.0 Hz), the amount of disconnected load is the same for power deficits in the range from 0 to 20 MW. L-UFLS disconnects less load in 37.03% and $UFLS_{10}$ in 27.16% of the cases compared to $UFLS_{50}$.

We are interested in the L-UFLS efficiency when the dynamic stage is activated. Fig. 19 shows the boxplot diagram of maximum frequency and *ROCOF* after the last UFLS intervention for power deficits greater than 20 MW. It can be seen that the greater the number of static stages is, the smaller the maximum frequency and *ROCOF* are. The results show that L-UFLS efficiency can be classified between $UFLS_{10}$ and $UFLS_{50}$. *We can therefore conclude that a L-UFLS with three sub-stages alongside a six-stage conventional UFLS corresponds to the results delivered by the conventional UFLS scheme with dozens of stages.*

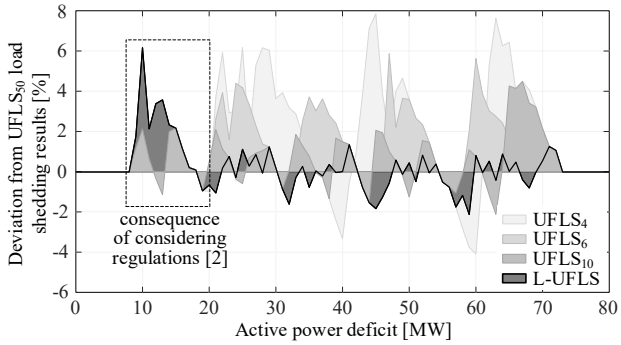

Fig. 18. Deviation from 50-stage UFLS total load shedding amount

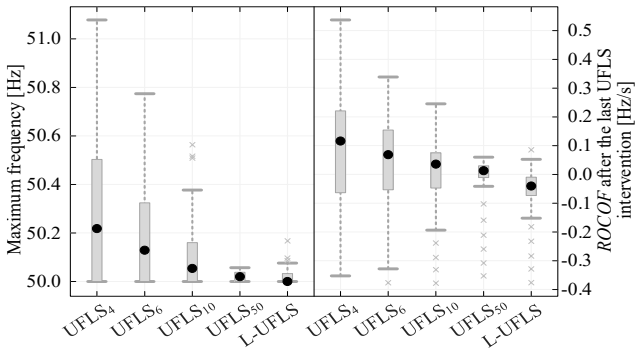

Fig. 19. Boxplot diagram of maximum frequency during the frequency transient and *ROCOF* after the last UFLS intervention

D. Comparison to another advanced solution following similar targets

The process of dynamic shifting of L-UFLS appears as if one would be dealing with a large number of conventional UFLS stages. A comparison to those is presented in Section IV.C. However, it is reasonable to compare L-UFLS efficiency with an *advanced* method that follows a similar (but unfortunately not equal) philosophy and targets as L-UFLS. For this purpose, we selected [43], which we dub M-UFLS. The notation originates from the core idea of defining frequency-stability margin variable $M(t)$. Before we compare the results, an important difference between both methods should be stressed. L-UFLS is subject to an intentionally imposed limitation that prevents it to modify conventional UFLS settings (in [43], conventional UFLS is subject to modification). We designed L-UFLS to operate alongside conventional UFLS in order to simplify its implementation and make it more cost-effective [43].

Fig. 20 and Fig. 21 depict the total load shedding amounts (Fig. 20) and minimal/maximal frequency values recorded during the transient (Fig. 21) for the same 80 MW active-power deficit values as in section IV.A.. We can observe that M-UFLS is able to achieve frequency stabilization with less disconnected load, but at the same time, it allows the frequency to temporary drop lower during the transient. This is not something we decided to allow in our solution. Instead, our intention was to fully stabilize the frequency with L-UFLS and not share this burden with frequency control. This is why L-UFLS decreases *ROCOF* after the last intervention much closer to zero than M-UFLS. Therefore, the comparison results highlight the fact that even the smallest and seemingly less important limitations can cause noticeable changes in UFLS efficiency. Since L-UFLS and M-UFLS do not have the exact same goals, results are appropriately different. Nevertheless, the philosophies of L-UFLS and M-UFLS are still extremely similar, much more similar than other solutions from the available literature. It should also be kept in mind that as a result, L-UFLS is associated with significantly lower implementation costs compared to M-UFLS, since it does not assume any intervention into existing conventional UFLS. Despite this, we can estimate that both solutions are well below the implementation cost of other complex solutions available in the existing literature (e.g. WAMS-based).

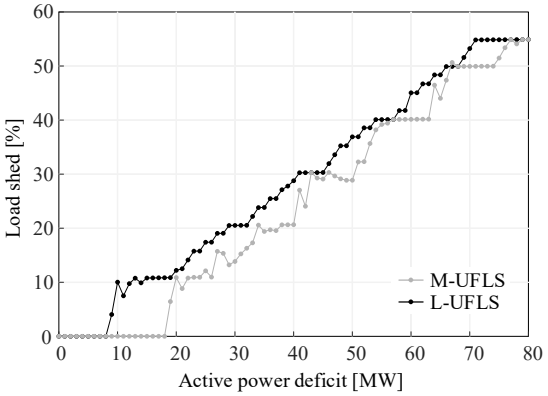

Fig. 20. Performance comparison of conventional L-UFLS and M-UFLS (total load shedding)

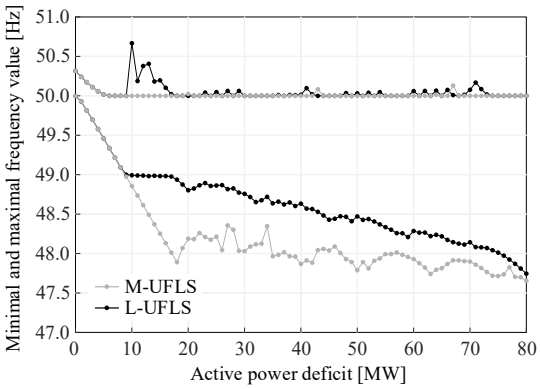

Fig. 21. Performance comparison of conventional L-UFLS and M-UFLS (minimum and maximum frequency values)

E. Operation under cascade tripping conditions

L-UFLS is predicted to actively participate in load shedding whenever certain conditions are met (i.e. frequency drop, *ROCOF* is low enough and loads are still available for shedding), regardless of the pre-existing situation. To show that system benefits from this under cascade-tripping conditions, the reader is asked to study Fig. 22. In Fig. 22 the EPS frequency response is depicted after two subsequent power imbalances (the first at t = 1 sec due to islanding and the second at t = 10 sec resulting from a generation unit trip). The black curve is showing the results corresponding to L-UFLS and the grey curve considers a conventional standalone 6-stage UFLS.

Initial power imbalance after islanding equals 74 MW. In order to solve this power imbalance, conventional UFLS trips four stages (in total 40% load decrease). On the other hand, L-UFLS allows only three conventional stages to be activated. Before the frequency reaches the threshold of the fourth stage, a single L-UFLS dynamic stage is activated that is sufficient to stop the frequency decay (in total 33.3% load decrease). It is obvious that after the frequency starts to recover, conventional UFLS causes significant overshoot, which is not the case with L-UFLS.

After the second imbalance at t = 10 sec, frequency starts to decrease again. Frequency thresholds of the remaining unused conventional UFLS are located at 48.2 Hz and 48.1 Hz, but they were not activated since the primary frequency control was able to stabilize the frequency by itself. On the other hand, L-UFLS has again recognized favourable conditions before the frequency reached the 4th static stage. This added 5% to system de-loading, which resulted in smooth frequency stabilization.

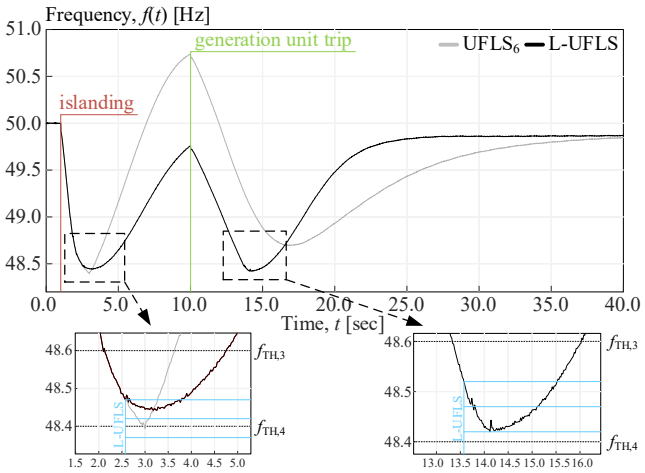

Fig. 22. Efficient operation under cascade tripping conditions

F. Operation uncertainties in power generation

The existing EPS trends and forecasts indicate a sharp decline in conventional generation on one hand and an increase in inverter-based generation (several of them intermittent in nature due to dependency on weather conditions) on the other. There are two resulting consequences: *i*) rotational kinetic energy, inherently a part of synchronous generators (overall EPS inertia) in operation, is expected to decrease and *ii*) inertia of the EPS will vary due to the intermittency of renewable energy sources.

We addressed both issues in the L-UFLS design process by assuring continuous frequency monitoring, splitting L-UFLS into several stages (three in this paper), using a frequency signal as an input rather than *ROCOF* and running the SFR fitting process on a wide sliding window, which neutralizes all random factors, such as noise and generation intermittency. For this purpose, we used a large-scale network from Section IV.B. to obtain three sets of simulations, with each set having different overall inertia in the system (0.5H, H, and 2H, where H is the actual inertia value of the Slovenian power system). Results are presented in Fig. 23 as a deviation from the conventional UFLS operation. The left plots show the difference between the total disconnection amount and the right plots show the difference in the maximum achieved frequency during the transient. We see that L-UFLS disconnects a smaller (up to about 5%) amount of load than conventional UFLS, regardless of the magnitude of inertia. When L-UFLS is used, the maximum frequencies are understandably lower at higher H, since by their nature, high-inertia networks are less vulnerable to frequency oscillations. On the other hand, similar results can be observed when inertia is halved. This confirms that the L-UFLS setting and its operation is independent of the uncertainties in power generation.

V. Conclusion

This paper proposes an improvement to the conventional UFLS scheme. The proposed solution retains the existing UFLS relay settings (tripping thresholds) and introduces an additional dynamic UFLS stage by means of a small and specialized group of IEDs equipped with machine-learning functionality. The libero UFLS is divided into a few sub-stages, the triggering criteria for which are automatically set. Pattern-recognition mechanism of the IEDs provides the awareness for the need to fine-tune the power-imbalance. This approach maintains the speed and robustness of conventional UFLS and provides the

desired flexibility at the same time. Research shows that the libero UFLS with three self-adjusting sub-stages is equivalent to the conventional UFLS with dozens of fixed stages. Compared to other existing advanced methods, its implementation in EPS is less intrusive and does not require wide-area communication. In fact, unsynchronised IED operation has several beneficial effects.

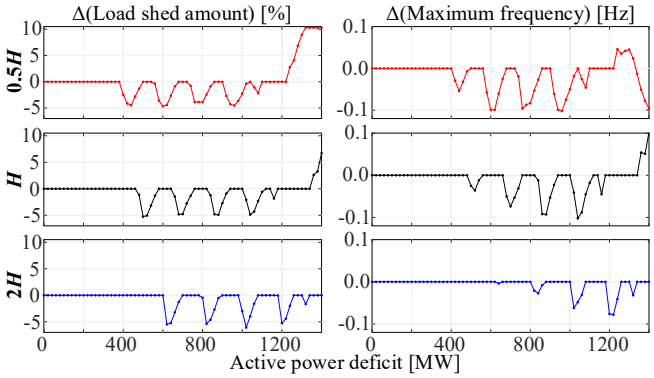

Fig. 23. Analysis of inertia impact on L-UFLS performance

VI. References

[1] S. Matthewman, H. Byrd, "Blackouts: a sociology of electrical power failure," *Soc. Space J.*, pp. 1-25, Jan. 2014.

[2] ENTSO-E, "RG CE OH – Policy 5: Emergency Operations V 3.1," Sep. 2017.

[3] H. H. Alhelou, M. E. H. Golshan, T. C. Njenda, P. Siano, "A Survey on Power System Blackout and Cascading Events: Research Motivations and Challenges," *Energies*, Vol. 12, No. 4, Feb. 2019.

[4] L. Sigrist, L. Rouco, F. M. Echavarren, "A review of the state of the art of UFLS schemes for isolated power systems," *Electr. Power and Energy Syst.*, Vol. 99, pp. 525-539, Jul. 2018.

[5] M. Lu, W. A. W. ZainalAbidin, T. Masri, D. H. A. Lee, S. Chen, "Under-Frequency Load Shedding (UFLS) Schemes – A Survey," *Int. J. Appl. Eng. Res.*, Vol. 11, No. 1, Feb. 2016.

[6] H. H. Alhelou, M. E. H. Golshan, R. Zamani, M. P. Moghaddam, T. C. Njenda, P. Siano, M. Marzband, "An Improved UFLS Scheme based on Estimated Minimum Frequency and Power Deficit," 2019 IEEE Milan PowerTech, Milan, Italy, Jun. 2019.

[7] W. Yao, S. You, W. Wang, X. Deng, Y. Li, L. Zhan, Y. Liu, "A Fast Load Control System Based on Mobile Distribution-Level Phasor Measurement Unit," IEEE Trans. Smart Grid, Vol. 11, No. 1, Jan. 2020.

[8] G. Wang, H. Xin, D. Gan, N. Li, Z. Wang, "An Investigation into WAMS-based Under-Frequency Load Shedding," 2012 IEEE Power and Energy Soc. Gen. Meeting, San Diego, CA, USA, Jul. 2012.

[9] F. Zare, A. Ranjbar, F. Faghihi, "Intelligent topology-oriented LS scheme in power systems integrated with high wind power penetration," IET Gener., Transm. Distrib., Vol. 14, No. 9, May 2020.

[10] M. Prasad, K. N. Satish, K. Sodhi, R. Sodhi, "A Synchrophasor Measurements based Adaptive Underfrequency Load Shedding Scheme," IEEE Innovative Smart Grid Technol. - Asia (ISGT-Asia), May 2014.

[11] J. A. Laghari, S. A. Almani, H. Mokhlis, J. Kumar, A. H. A. Bakar, "A Smart Under-Frequency Load Shedding Scheme based on Takagi-Sugeno Fuzzy Inference System and Flexible Load Priority," (IJACSA) Int. J. of Adv. Comput. Sci. Appl., Vol. 9, No. 3, 2018.

[12] D. Lopez, L. Sigrist, "A Centralized UFLS Scheme Using Decision Trees for Small Isolated Power Systems," IEEE Latin America Trans., Vol. 15, No. 10, Oct. 2017.

[13] K. Mehrabi, S. Afsharnia, S. Golshannavaz, "Toward a wide-area load shedding scheme: Adaptive determination of frequency threshold and shed load values," Int. Trans. Electr. Energy Syst., Vol. 28, No. 1, Oct. 2017.

[14] J. Wang, H. Zhang, Y. Zhou, "Intelligent Under Frequency and Under Voltage Load Shedding Method Based on the Active Participation of Smart Appliances," IEEE Trans. Smart Grid, Vol. 8, No. 1, Jan. 2017.

[15] L. Sigrist, I. Egido, L. Rouco, "Principles of a centralized UFLS scheme for small isolated power systems," IEEE Trans. Power Syst., Vol. 28, No. 2, May 2013.

[16] Y. Xu, W. Liu, J. Gong, "Stable Multi-Agent-Based Load Shedding Algorithm for Power Systems," IEEE Trans. on Power Syst., Vol. 26, No. 4, Nov. 2011.

[17] B. Hoseinzadeh, F. M. F. Silva, C. L. Bak, "Adaptive Tuning of Frequency Thresholds Using Voltage Drop Data in Decentralized Load Shedding," IEEE Trans. Power Syst., Vol. 30, No. 4, Jul. 2015.

[18] C. Li, Y. Wu, Y. Sun, H. Zhang, Y. Liu, Y. Liu, V. Terzija, "Continuous Under-Frequency Load Shedding Scheme for Power System Adaptive Frequency Control," IEEE Trans. Power Syst., Vol. 35, No. 2, Mar. 2020.

[19] D. L. H. Aiu, "A General-Order System Frequency Response Model Incorporating Load Shedding: Analytic Modeling and Applications," IEEE Transactions on Power Systems, Vol. 21, No. 2, May 2006.

[20] B. Potel, V. Debusschere, F. Cadoux, U. Rudez, "A real-time adjustment method of conventional under-frequency load shedding thresholds," IEEE Trans. Power Deliv., Vol. 34, No. 9, Dec. 2019.

[21] L. Jenkins, "Optimal load shedding algorithm for power system emergency control," 1983 Proceedings of the International Conference on Systems, Man and Cybernetics, Bombay and New Delhi, India, 1983.

[22] Y. Halevi, D. Kottick, "Optimization of load shedding system," IEEE Trans. Energy Convers., Vol. 8, No. 2, Jun. 1993.

[23] F. Ceja-Gomez, S. S. Qadri, F. D. Galiana, "Under-Frequency Load Shedding Via Integer Programming," IEEE Trans. Power Syst., Vol. 27, No. 3, Aug. 2012.
[24] J. A. P. Lopes, W. Wong Chan, L. M. Proenca, "Genetic Algorithms in the Definition of Optimal Load Shedding Strategies," PowerTech Budapest 99, Budapest, Hungary, Aug.-Sep. 1999.
[25] M. A. Mitchell, "Optimization of under-frequency load shedding strategies through the use of a neural network and a genetic algorithm," In: INESC, Vol. Master: Universidade do Porto; 2000.
[26] C. R. Chen, T. Wen-Ta, H. Y. Chen, L. Ching-Ying, C. Chun-Ju, L. Hong-Wei, "Optimal Load Shedding Planning with Genetic Algorithm," IEEE Industry Applications Society Annual Meeting (IAS), Nov. 2011.
[27] Y. Y. Hong, S. F. Wei, "Multiobjective Underfrequency Load Shedding in an Autonomous System Using Hierarchical Genetic Algorithms," IEEE Trans. Power Deliv., Vol. 25, No. 3, Jul. 2010.
[28] P. M. Anderson, M. Mirheydar, "A Low-Order System Frequency Response Model," IEEE Trans. Power Syst., Vol. 5, No. 3, Aug. 1990.
[29] P. Etingov, Z. Hou, H. Wang, H. Ren, "Cloud Based Analytical Framework for Synchrophasor Data Analysis," CIGRE Grid of the Future Symposium, Cleveland, Ohio, USA, Nov. 2017.
[30] A. Arunan, J. Ravishankar, E. Ambikariajah, "Improved disturbance detection and load shedding technique for low voltage islanded microgrids," IET Gener. Transm. Distrib., Vol. 13, No. 11, Apr. 2019.
[31] A. Derviskadic, Y. Zuo, G. Frigo, M. Paolone, "Under Frequency Load Shedding based on PMU Estimates of Frequency and ROCOF," 2018 IEEE Innovative Smart Grid Technol. - Europe (ISGT-Europe), Oct. 2018.
[32] Y. Zhu, C. Liu, K. Sun, "Image Embedding of PMU Data for Deep Learning towards Transient Disturbance Classification," IEEE Int. Conf. on Energy Internet (ICEI), Beijing, China, May 2018.
[33] R. O. Duda, P. E. Hart, D. G. Stork, "Pattern Classification", 2nd Edition, New York, NY, USA: John Wiley & Sons, Inc, 2001.
[34] S. B. Mohammed, A. Khalid, S. E. F. Osman, R. G. M. Helali, "Usage of Principal Component Analysis (PCA) in AI Applications," Int. J. Eng. Res. Technol. (IJERT), Vol. 5, No. 12, Dec. 2016.
[35] C. M. Bishop, Pattern recognition and machine learning, New York, NY, USA: Springer-Verlag, 2006.
[36] U. Rudez, R. Mihalic, "Monitoring the First Frequency Derivative to Improve Adaptive Underfrequency Load-Shedding Schemes," IEEE Trans. Power Syst., Vol. 26, No. 2, May 2011.
[37] ENTSO-E, "Frequency Measurement Requirements and Usage – Final Version 7," RG-CE System Protection & Dynamics Sub Group, ENTSO-E: Brussels, Belgium, 2018.
[38] Y. Guo, K. Li, D. M. Laverty, Y. Xue, "Synchrophasor-Based Islanding Detection for Distributed Generation Systems Using Systematic Principal Component Analysis Approaches," IEEE Trans. Power Deliv., Vol. 30, No. 6, Dec. 2015.
[39] P. Kundur, Power System Stability and Control, 1st edition, New York: McGraw-Hill, 1994.
[40] H. Huang, P. Ju, Y. Jin, X. Yuan, C. Qin, X. Pan, X. Zang, "Generic System Frequency Response Model for Power Grids with Different Generations," IEEE Access, Vol. 8, pp. 14314-14321, Jan. 2020.
[41] M. Raginsky, "Lecture XV: Inverse Laplace transform," BME 171: Signals and Systems, Duke University, Nov. 2018.
[42] D. Kopse, U. Rudez, R. Mihalic, "Applying a wide-area measurement system to validate the dynamic model of a part of European power-system," Electr. Power Syst. Res., Vol. 119, pp. 1-10, Feb. 2015.
[43] D. Sodin, R. Ilievska, A. Čampa, M. Smolnikar, U. Rudez, "Proving a Concept of Flexible Under-Frequency Load Shedding with Hardware -in-the-Loop Testing," *Energies*, Vol. 13, pp. 3607, Jul. 2020.